Journal of Physics:
Condensed Matter

PAPER

Challenges in magnetic modulation of 2D materials: exemplified with MoS_2

To cite this article: Sen Wang *et al* 2025 *J. Phys.: Condens. Matter* **37** 265801

IOP Publishing Journal of Physics: Condensed Matter
J. Phys.: Condens. Matter **37** (2025) 265801 (17pp) https://doi.org/10.1088/1361-648X/ade2ca

Challenges in magnetic modulation of 2D materials: exemplified with MoS_2

Sen Wang, Jia-Yi Lin and Yu-Jun Zhao*

Department of Physics, South China University of Technology, Guangzhou 510640, People's Republic of China

E-mail: zhaoyj@scut.edu.cn

Received 3 November 2024, revised 29 May 2025
Accepted for publication 9 June 2025
Published 19 June 2025

Abstract

In recent years, the rapid advancement of integrated circuit technology and electronic devices has positioned two-dimensional (2D) materials as promising candidates for next-generation spintronic devices, owing to their reduced dimensions and lower energy dissipation. Despite these advantages, the majority of 2D materials are intrinsically non-magnetic. To overcome this limitation and expand the application of 2D materials in spintronics, various strategies have been developed to introduce ferromagnetic properties into non-magnetic systems. In this study, we provide a comprehensive review of recent efforts to regulate the magnetic properties of 2D non-magnetic materials through heteroatom doping. Using monolayer MoS_2 doped with six different elements (V, Mn, Fe, Ni, Cu, and N) as a case study, we apply first-principles calculations to evaluate the feasibility of doping-induced magnetism by analyzing doping concentration, electronic structure stability, and the emergence of long-range magnetic order. Our findings reveal that magnetic regulation in 2D materials presents significant challenges. For theoretical researchers aiming to practically support experimental investigations into magnetic modulation in 2D materials, it is crucial to consider the following three key questions: (i). Can the desired concentration of doped atoms be successfully achieved? (ii). Do these doped atoms exhibit localized magnetic moments? (iii). Is there evidence of long-range magnetic ordering among the magnetic moments of the doped atoms?

Keywords: two-dimensional materials, theoretical simulations, heteroatom doping, magnetic regulation

1. Introduction

With the rapid advancement of internet science and technology, along with the continuous miniaturization of chip sizes, traditional semiconductor devices are increasingly inadequate to meet the demands of modern life and industrial production [1]. In contrast, novel spintronic devices offer several significant advantages, including minimal heat dissipation, high storage density, and rapid data processing capabilities. These characteristics position spintronics as a promising technology poised to overcome the limitations of conventional semiconductor devices [2–4].

Since the successful isolation of two-dimensional (2D) graphene in 2004 [5], research on 2D spintronic devices has intensified. Recent studies have reported the emergence of long-range ferromagnetic order in materials such as 2D $Cr_2Ge_2Te_6$[6], Fe_3GeTe_2[7], Fe_4GeTe_2[8], CrI_3[9], and $CrBr_3$[10]. However, the limited availability of intrinsic 2D magnetic materials, coupled with their typically low Curie temperatures-often well below room temperature-poses significant challenges for practical applications. The Mermin–Wagner theorem states that in the isotropic Heisenberg model, continuous symmetry cannot undergo spontaneous breaking at finite temperatures for systems with dimensions $d \leqslant 2$

* Author to whom any correspondence should be addressed.

characterized by sufficiently short-range interactions, which fundamentally accounts for the inherent challenge in achieving long-range magnetic order in 2D systems [11]. Notably, enhanced magnetic anisotropy has been recognized as an effective mechanism to suppress random spin reorientations induced by thermal fluctuations, thereby establishing a feasible pathway for realizing 2D magnetic phenomena.

Fortunately, researchers have developed multiple viable strategies to induce ferromagnetism in intrinsically non-magnetic 2D materials, including defect engineering [12–14], heterostructure coupling [15–17], heteroatom doping [18–20], and chemical intercalation [21–23]. These four approaches are collectively termed structural engineering methods. Structural engineering enables magnetic modulation that can be categorized into two classes: (1) introducing long-range magnetic order in intrinsically non-magnetic materials (intrinsic modification); (2) modifying existing magnetism in intrinsically magnetic materials to tune Curie temperature and magnetocrystalline anisotropy energy. This review focuses exclusively on the first scenario, excluding room-temperature long-range ferromagnetism studies. To illustrate this approach, we examine defect engineering mechanisms: defects may form intrinsically during 2D material growth or be deliberately introduced via post-synthesis treatments. Beyond modulating fundamental physicochemical properties (e.g. electronic band structure and catalytic activity), defects are capable of inducing local spin polarization and establishing ferromagnetic ordering in otherwise non-magnetic 2D systems. However, defect formation is often challenging to precisely control and may cause irreversible damage to the intrinsic properties of materials. Therefore, further research is required to achieve effective and tunable defect engineering. Heterostructure coupling leverages the magnetic proximity effect, where interfacial exchange interactions with adjacent ferromagnetic materials enable the emergence of ferromagnetism in the coupled non-magnetic 2D components. This approach offers the advantage of preserving the intrinsic structure of the material, allowing magnetic modulation without compromising its inherent properties. Heteroatom doping involves the substitutional incorporation of magnetic or non-magnetic elements, fundamentally reconstructing the host material's electronic structure through modifications in the *d*-orbital density of states (DOSs). This strategy provides a feasible pathway for achieving synergistic coupling between magnetic properties and optical, electrical, and mechanical characteristics. However, achieving high doping concentrations while maintaining large-scale uniformity in 2D materials remains a significant challenge. Chemical intercalation of foreign species into the van der Waals interlayers serves as a powerful platform for precisely engineering the host material's electronic, optical, and magnetic properties via controlled interlayer charge/spin redistribution. The reversible nature of magnetism induced in certain intercalated materials holds significant potential for non-volatile programmable logic devices. Notably, for non-layered 2D materials that are difficult to synthesize directly, intercalation offers an effective preparation route-enabling synthesis by embedding atoms into the interstices of layered templates. For example, layered SnS_2 can serve as a 2D template to produce non-layered 2D Cu_2SnS_3 [24]. Additionally, self-intercalation techniques, through the modulation of elemental ratios, provide a novel approach for broad-range tuning of magnetic parameters in 2D materials. These strategies are crucial for expanding the family of 2D magnetic materials and promoting their practical utilization. For instance, although graphene is inherently non-magnetic, it can generate localized magnetic moments through defects such as surface atom adsorption [12, 13, 25, 26], dislocations [27, 28], and zigzag edges [29, 30]. Besides, heterostructure coupling (e.g. graphene/CrSBr [16], graphene/EuO [31] and graphene/EuS [17]) and chemical intercalation (e.g. $FeCl_3$-intercalated few-layer graphene [32] and Eu-intercalated few-layer graphene [33]) can also induce spin polarization.

A detailed summary of recent efforts to induce ferromagnetism in 2D non-magnetic materials through heteroatom doping is provided in appendix B: table B1. As outlined in the table, theoretical investigations have established that heteroatom doping constitutes an effective strategy for modulating the magnetic properties of 2D non-magnetic materials, although the number of successful experimental cases remains limited. Furthermore, it indicates that the magnetic moments per unit molecular formula in these experimentally validated instances are significantly low [34–36]. Indeed, the practical applications of tuning the magnetic properties of 2D materials via heteroatom doping are relatively sparse.

Our research seeks to uncover the fundamental reasons behind the discrepancies between theoretical predictions and experimental results by analyzing three critical factors: (1) can the doped atoms achieve the desired concentration? (2) Do the doped atoms exhibit localized magnetic moments? (3) Is long-range magnetic order established between the magnetic moments of the doped atoms? Transition metal dichalcogenides (TMDCs) have garnered considerable research interest owing to their versatile applications in optoelectronics, electronics, photocatalysis, magnetic switching devices, and information storage technologies [37–42]. Among these, molybdenum disulfide (MoS_2), which possesses a direct bandgap, emerges as a promising candidate for optoelectronic and photocatalytic applications [43–45]. The material's appeal is further enhanced by its facile doping capability and compatibility with heterostructure engineering, which endows it with tunable and desirable properties, positioning MoS_2 as a competitive alternative to graphene. In this study, we focus on monolayer 1 H-MoS_2 to systematically investigate magnetic modulation via substitutional doping with six distinct elements (V, Mn, Fe, Ni, Cu, and N). Computational methodologies are comprehensively described in appendix A. Based on precise theoretical simulations, we find that achieving long-range magnetic order in MoS_2 doped with V, Fe, Ni, Cu, or N is highly challenging. Among these dopants, Mn-doped MoS_2 exhibits the greatest potential for successful magnetic regulation; however, the clustering tendency of Mn atoms must be taken into account. These findings underscore the significant challenges in regulating the magnetism of 2D non-magnetic materials through heteroatom doping.

In addition to the six doping elements examined in this work, current studies demonstrate that cobalt (Co) doping can also regulate the magnetic properties of MoS_2. Theoretical calculations [40, 46–48] suggest that Co doping induces ferromagnetic ordering, while experimental investigations [49, 50] on hydrothermally synthesized samples have detected weak magnetic signals, though these observations remain ambiguous due to potential contributions from magnetic clusters or secondary phases. From a purely theoretical perspective, Cheng *et al* [51] utilized first-principles calculations to confirm the thermodynamic stability of Zn-, Cd-, and Hg-doped systems through binding energy analysis, further predicting the emergence of a ferromagnetic ground state in these configurations. Separately, Majid *et al* [52] explored the magnetic behavior of rare-earth-element-doped (Sm, Eu, Gd, Tb, Dy) monolayer MoS_2, reporting localized magnetic moments of 3.3 μ_B, 8.1 μ_B, 8.5 μ_B, 6.8 μ_B and 6.4 μ_B, respectively; however, their work did not address the structural stability of doped systems or the underlying magnetic coupling mechanisms. Nonmetallic dopants (H, B, F)[53, 54] have similarly been shown to generate localized magnetic moments in MoS_2, yet systematic investigations into their magnetic coupling interactions remain absent. Beyond the MoS_2 system, transition metal atom doping has been shown to induce ferromagnetism in graphene [55], TMDCs (e.g. $MoSe_2$)[56, 57], metal oxides (e.g. SnO_2)[58], phosphorene [59], and silicene [60]. Likewise, non-metal atom doping (e.g. S, N) in graphene [61] and carbon (C)-doped hexagonal boron nitride [62] can also impart ferromagnetic ordering. Crucially, the majority of these findings are confined to computational predictions, with experimental verification and practical implementation still posing substantial challenges. Additionally, we conducted separate calculations for Mn-, Fe-, and N-interstitial doping configurations in monolayer MoS_2, with computed defect formation energies all approximately 4 eV. This quantitatively confirms the exceptionally low thermodynamic stability of these elements at interstitial lattice sites. Our conclusion is fully consistent with the seminal work by Onofrio *et al* [63]., thereby providing rigorous justification for excluding interstitial doping configurations from our theoretical models.

2. Results and discussion

2.1. Doping concentration

When investigating the introduction of magnetism into 2D non-magnetic materials via heteroatom doping, stability analysis is paramount. The first step involves assessing the thermal stability of the doped system and estimating the doping concentration. Subsequently, the electronic structure stability must be examined to determine whether the system exhibits localized magnetic moments. Finally, the magnetic coupling between dopant atoms needs to be evaluated to ascertain whether the system demonstrates long-range magnetic order on a macroscopic scale.

The formation energy of defects is a crucial indicator of the thermal stability of the doped system; lower formation energy implies that defects are more likely to form. The expression for the formation energy of point defects is [64, 65]:

$$\Delta H_{\mathrm{f}} = E_{\mathrm{D}} - E_{\mathrm{H}} + \sum n_\alpha \mu_\alpha + q\left(E_{\mathrm{VBM}} + E_{\mathrm{F}}\right), \qquad (1)$$

where E_{D} and E_{H} are the total energies of the system with and without defects, respectively. n_α is the number of defect atoms, which is negative when atoms are added to the ideal system and positive when atoms are removed from the ideal system. μ_α is the absolute value of the chemical potential of atom α, which can be defined as $\mu_\alpha = \mu_\alpha^{\mathrm{bulk}} + \Delta\mu_\alpha$, where $\mu_\alpha^{\mathrm{bulk}}$ represents the chemical potential of an elemental solid in its stable form. q denotes the valence state of the α atom, E_{VBM} represents the energy of the valence band maximum (VBM) of the system in the absence of defects, and E_{F} is the Fermi level relative to E_{VBM}. To induce macroscopic magnetic order in 2D materials, a relatively high doping concentration is essential. Nevertheless, preserving the electrical neutrality of the sample rules out the possibility of introducing charged defects. Consequently, in this study, we assume $q = 0$.

Typically, the formation energy of defects in materials is positive; otherwise, the stability of the pristine crystal would not be maintained. However, numerous studies have reported negative defect formation energies [46, 53, 66–73], which is clearly not physically reasonable. The primary reason for the calculation of negative defect formation energies in these studies is the erroneous selection of the atomic chemical potential, μ_α. Furthermore, some studies reported exceptionally high defect formation energies, with minimum values as large as 5.5 eV [74] and 3.61 eV [75], which correspond to extremely low thermal equilibrium concentrations of dopant atoms, thereby making it challenging to achieve macroscopic magnetism. In addition, several studies assess the stability of defect systems by considering the binding energy [51, 54, 76–87]. Certain studies bypass the analysis of the thermodynamic stability of doped systems and directly examine the physical properties of non-magnetic materials after doping at specific concentrations [88–91]. These methods raise concerns that the doped systems under investigation might be thermodynamically unstable.

In order to facilitate further in-depth research into the control of the magnetism of 2D materials through defect modulation, it is essential to first undertake an accurate calculation of the defect formation energy in doped systems. The defect formation energy can be employed to estimate the thermal equilibrium site concentration of defects, as demonstrated by the following formula:

$$[\mathrm{defect}] = \exp\left(-\Delta H_{\mathrm{f}}/kT\right), \qquad (2)$$

where ΔH_{f} is the defect formation energy, k is the Boltzmann constant, and T is the melting point of the crystal. Typically, when the calculated thermal equilibrium site concentration is very low, the distance between the dopant atoms is large, making it difficult to modulate the macroscopic magnetism of the doped system.

The following example, where a Mn atom is used to substitute a single-layer $5\times5\times1$ MoS_2 supercell, provides a detailed

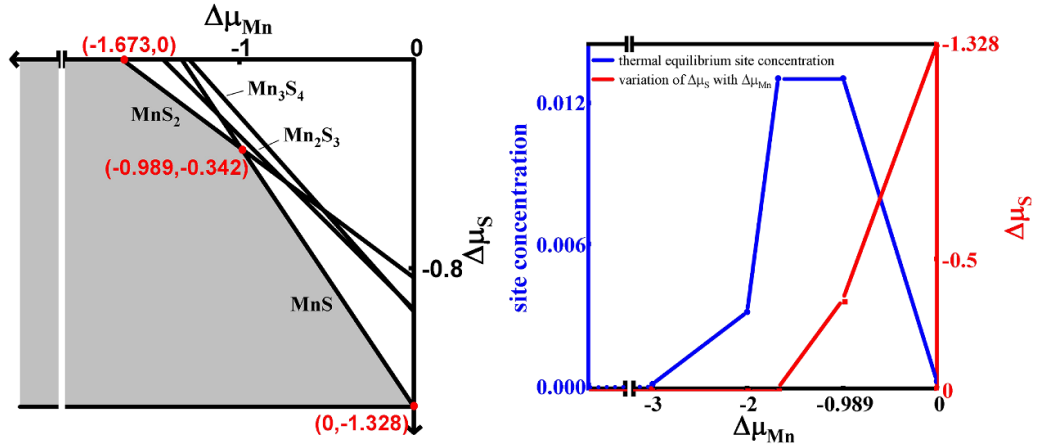

Figure 1. (a) The final permissible region (shaded) for $\Delta\mu_{\mathrm{Mn}}$ corresponding to $\Delta\mu_{\mathrm{S}}$ in the ($\Delta\mu_{\mathrm{Mn}}$, $\Delta\mu_{\mathrm{S}}$) plane for Mn-doped MoS_2. (b) The red curve illustrates the relationship between variables $\Delta\mu_{\mathrm{S}}$ and $\Delta\mu_{\mathrm{Mn}}$. The blue curve represents the thermodynamic equilibrium site concentration, calculated based on the principles of thermodynamic equilibrium.

explanation of the defect formation energy calculation through three main steps.

(i) In order for a stable MoS_2 structure to be formed, the following condition must be satisfied:

$$\Delta\mu_{\mathrm{Mo}} + 2\Delta\mu_{\mathrm{S}} = \Delta H(\mathrm{MoS_2}). \tag{3}$$

(ii) In order to prevent the precipitation of elemental substances, the following condition must be satisfied:

$$\Delta\mu_{\mathrm{Mo}} \leqslant 0,\ \Delta\mu_{\mathrm{S}} \leqslant 0. \tag{4}$$

From equations (3) and (4), one can ascertain the range of $\Delta\mu_{\mathrm{Mo}}$ and $\Delta\mu_{\mathrm{S}}$ required for the stable formation of MoS_2, with $\Delta\mu_{\mathrm{S}}$ is constrained to values between -1.328 eV and 0 eV.

(iii) In order to prevent the emergence of competing phases, it is necessary that $\Delta\mu_{\mathrm{Mo}}$ and $\Delta\mu_{\mathrm{S}}$ also satisfy the following condition:

$$\Delta\mu_{\mathrm{Mn}} \leqslant 0, \tag{5}$$
$$\Delta\mu_{\mathrm{Mn}} + \Delta\mu_{\mathrm{S}} \leqslant \Delta H_{\mathrm{f}}(\mathrm{MnS}), \tag{6}$$
$$\Delta\mu_{\mathrm{Mn}} + 2\Delta\mu_{\mathrm{S}} \leqslant \Delta H_{\mathrm{f}}(\mathrm{MnS_2}), \tag{7}$$
$$2\Delta\mu_{\mathrm{Mn}} + 3\Delta\mu_{\mathrm{S}} \leqslant \Delta H_{\mathrm{f}}(\mathrm{Mn_2S_3}), \tag{8}$$
$$3\Delta\mu_{\mathrm{Mn}} + 4\Delta\mu_{\mathrm{S}} \leqslant \Delta H_{\mathrm{f}}(\mathrm{Mn_3S_4}). \tag{9}$$

According to equations (4)–(9), figure 1(a) can be plotted. As illustrated in figure 1(a), during the formation of MoS_2, it is essential to avoid the emergence of competitive phases while maintaining stability. Consequently, the chemical potentials of manganese and sulfur atoms must remain within the shaded region, with the boundary delineating the critical values of permissible chemical potentials. The calculation of defect formation energy can be expressed as follows:

$$\begin{aligned}\Delta H_{\mathrm{f}} &= E_{\mathrm{D}} - E_{\mathrm{H}} + \mu_{\mathrm{Mo}} - \mu_{\mathrm{Mn}} \\ &= E_{\mathrm{D}} - E_{\mathrm{H}} + \left(\mu_{\mathrm{Mo}}^{\mathrm{bulk}} + \Delta H(\mathrm{MoS_2}) - 2\Delta\mu_{\mathrm{S}}\right) \\ &\quad - \left(\mu_{\mathrm{Mn}}^{\mathrm{bulk}} + \Delta\mu_{\mathrm{Mn}}\right).\end{aligned} \tag{10}$$

Using equations (3)–(10), the defect formation energy of Mn-doped MoS_2 as a function of $\Delta\mu_{\mathrm{Mn}}$ can be readily calculated. Starting from the minimum defect formation energy, Equation (2) allows for the determination of the corresponding equilibrium site concentration, as illustrated in figure 1(b). The figure reveals that the maximum thermal equilibrium site concentration for Mn-doped monolayer MoS_2 reaches 1.304%.

Following the aforementioned procedure, we systematically calculated the evolution of the defect formation energy with respect to the chemical potential for V-, Mn-, Fe-, Ni-, Cu-, and N-doped monolayer MoS_2 systems. By extracting the minimum formation energy for each system and incorporating the defect equilibrium concentration formula (equation (2)), we derived the maximum thermal equilibrium site concentrations for each doped system, as summarized in table 1. As shown in table 1, V, Mn, and N atoms can be doped into MoS_2 at relatively high concentrations, whereas the maximum equilibrium concentrations for Fe, Ni, and Cu doping are significantly lower. Therefore, based solely on thermodynamic stability analysis, it can be concluded that high-concentration doping of MoS_2 with Fe, Ni, and Cu atoms is unlikely. Consequently, the approach of modulating the magnetic properties of MoS_2 through Fe, Ni, and Cu doping is expected to face significant challenges.

2.2. *Electronic structure stability*

The ideal monolayer MoS_2 is a typical TMD with a space group $P\bar{6}m2$ (D_{3h} point group) and a honeycomb hexagonal lattice structure, where each molybdenum atom is surrounded by six sulfur atoms. In monolayer MoS_2, the Mo atom

Table 1. Theoretically calculated minimum formation energies (ΔH_f^{min}), maximum doping site concentrations ($[defect]_{max}$), and local magnetic moments (m) for different substituted dopants in monolayer MoS_2.

Impurity	ΔH_f^{min} (eV)	$[defect]_{max}$	$m\,(\mu_B/\text{impurity})$
V	0.277	2.969×10^{-1}	1
Mn	0.99	1.304×10^{-2}	1
Fe	2.046	1.272×10^{-4}	2
Ni	2.769	5.346×10^{-6}	0
Cu	3.665	1.052×10^{-7}	1
N	0.999	1.253×10^{-2}	1

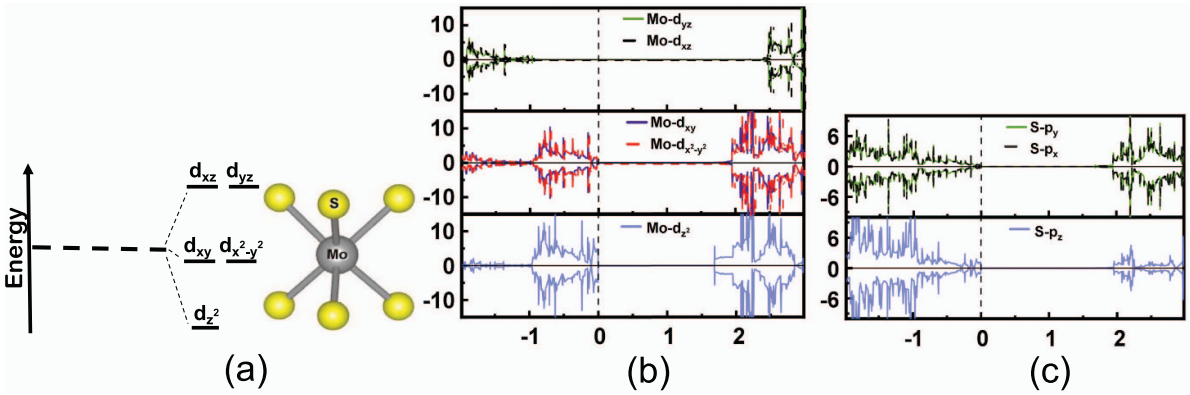

Figure 2. (a) Schematic of the energy splitting of Mo atoms d bands under the crystal field. The coordination is trigonal prismatic. (b) and (c) PDOS of a pristine (undoped) MoS_2 monolayer.

is coordinated in a trigonal prismatic arrangement with chalcogen atoms, as illustrated in figure 2(a). Within crystal field theory, the trigonal prismatic coordination of the Mo atom lifts the degeneracy of the Mo 4d energy levels. The d orbitals of the Mo atom split into three groups: the d_{xy} and $d_{x^2-y^2}$ orbitals form a doubly degenerate level due to in-plane symmetry, typically the highest in energy. The d_{xz} and d_{yz} degenerate orbitals are lower in energy due to weaker out-of-plane symmetry. The dz^2 orbital remains independent, with its electron cloud primarily distributed perpendicular to the plane, making it the lowest in energy [92, 93]. As illustrated in the figures 2(b) and (c), the projected DOSs (PDOS) of the Mo atom and S atom in MoS_2 aligns with the results predicted by crystal field theory. In the PDOS of the S atom, the p_x and p_y orbitals are doubly degenerate. The p_z orbital and the p_x and p_y orbitals have slightly different densities of states due to the differing symmetry of the S atom in the z-direction compared to the x and y directions. Experiments and first-principles calculations indicate that the d_{z^2}, d_{xy}, and $d_{x^2-y^2}$ orbitals of the Mo atom hybridize with the 3p orbitals of the S atom; these hybridized states contribute to the conduction and valence band edges of MoS_2 [92, 94–98].

To effectively induce magnetism in a non-magnetic material through doping, the doped system must exhibit a local magnetic moment.This study explores the local magnetism of a $5 \times 5 \times 1$ MoS_2 supercell doped with six elements: V, Mn, Fe, Ni, Cu, and N, utilizing precise computational methods. Notably, the total number of valence electrons in the V, Mn, Cu, and N-doped systems is odd, prompting additional supercell calculations to ascertain the magnetic moments of the double-doped systems. The results, summarized in table 1, show that doping with V, Mn, Fe, Cu, and N introduces local magnetic moments, while doping with Ni does not result in local magnetic moments.

Ni and Cu doping can induce Jahn–Teller distortion, which has a pronounced impact on the local magnetic moment. As illustrated in figure 3, the band structure and DOSs for Ni-doped MoS_2 are shown both before and after full relaxation. Figure 3(a) demonstrates that, prior to full relaxation, Ni doping induces spin polarization, with the impurity levels exhibiting significant spin-splitting energy. The four additional valence electrons of the Ni atom, compared to the Mo atom, occupy the lower energy spin-down states, thereby leading to the formation of local magnetic moments. From figure 3(b), it can be inferred that the d-orbitals of Ni exhibit two doubly degenerate states, which are likely to be unstable. Previous studies have reported that Ni substitutional doping in monolayer MoS_2 can introduce a local magnetic moment, with values potentially reaching up to 4 μ_B [72, 74], corresponding to the magnetic state observed prior to full relaxation, which is inherently unstable. After full relaxation, as depicted in figures 3(c) and (d), the system experiences a lifting of degeneracy, leading to the splitting of the d-orbitals into five spin-degenerate singlet states [51]. Consequently, the four additional electrons occupy the two lower-energy levels, resulting in a local magnetic moment of 0 μ_B.

The situation for Cu doping in monolayer MoS_2 is similar to that of Ni doping. As illustrated in figure 4, the band

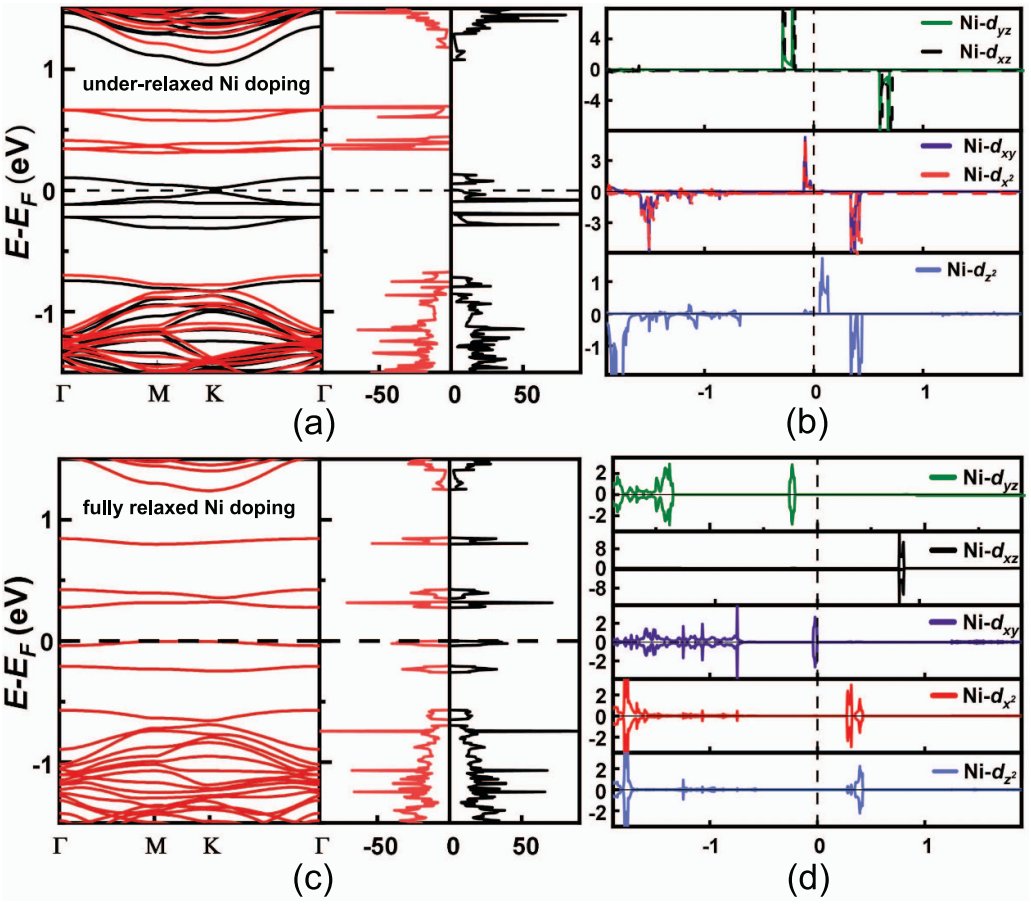

Figure 3. (a) and (c) Show band structures and DOSs for an under-relaxed and a fully relaxed Ni-doped monolayer of MoS_2. (b) and (d) Show the *d*-orbital PDOS of an under-relaxed and a fully relaxed Ni-doped monolayer of MoS_2.

structures and DOSs are depicted both before and after full relaxation for the Cu-doped MoS_2 system. Figure 4(a) reveals that, prior to full relaxation, Cu doping induces spin polarization, characterized by significant spin-splitting of impurity levels. The Cu atom, possessing five more valence electrons than the Mo atom, occupies five spin-down states, thereby generating a local magnetic moment of 5 μ_B. From figure 4(b), it can be inferred that the Cu *d*-orbitals present two doubly degenerate states, which are likely unstable. Previous studies have indicated that Cu substitutional doping in monolayer MoS_2 can introduce a strong local magnetic moment [46, 71, 72], corresponding to the magnetic state before full relaxation, which is inherently unstable. Upon full relaxation, as demonstrated in figures 4(c) and (d), the system undergoes a lifting of degeneracy, leading to a reduction in the degeneracy of the *d*-orbitals and a decrease in spin-splitting energy. Consequently, the additional five valence electrons occupy three spin-up states and two spin-down states, resulting in a local magnetic moment of 1 μ_B.

Although extensive research has been conducted on transition metal doping, the effects of non-metal doping on the magnetic properties of monolayer MoS_2 have received comparatively less attention. Several studies employing first-principles calculations have investigated the magnetism induced by non-metal atom doping, including elements such as H, B, N, and F [53, 54]. These non-metal dopants are capable of introducing a local magnetic moment, with all cases showing a local magnetic moment of 1 μ_B. Specifically, when a non-metal atom with an odd number of electrons dopes monolayer MoS_2, it inherently induces a local magnetic moment. The electrons of the non-metal atoms tend to pair up, leaving an unpaired valence electron, resulting in a calculated local magnetic moment of 1 μ_B. However, it is important to note that if the literature does not account for the magnetic coupling effects arising from either metal or non-metal [53, 54, 72] atom doping, the conclusions drawn about the introduction of magnetism via doping may be flawed, as the doped system may not exhibit macroscopic magnetism.

2.3. *Long-range magnetic ordering*

In regulating the magnetism of doped systems, it is necessary not only to analyze the doping concentration and localized magnetic moments, but also to consider the magnetic coupling between the two dopant atoms in the system, specifically whether long-range magnetism is present. Table 2 presents the magnetic coupling calculations of two heteroatoms substituted into monolayer MoS_2 ($5 \times 5 \times 1$

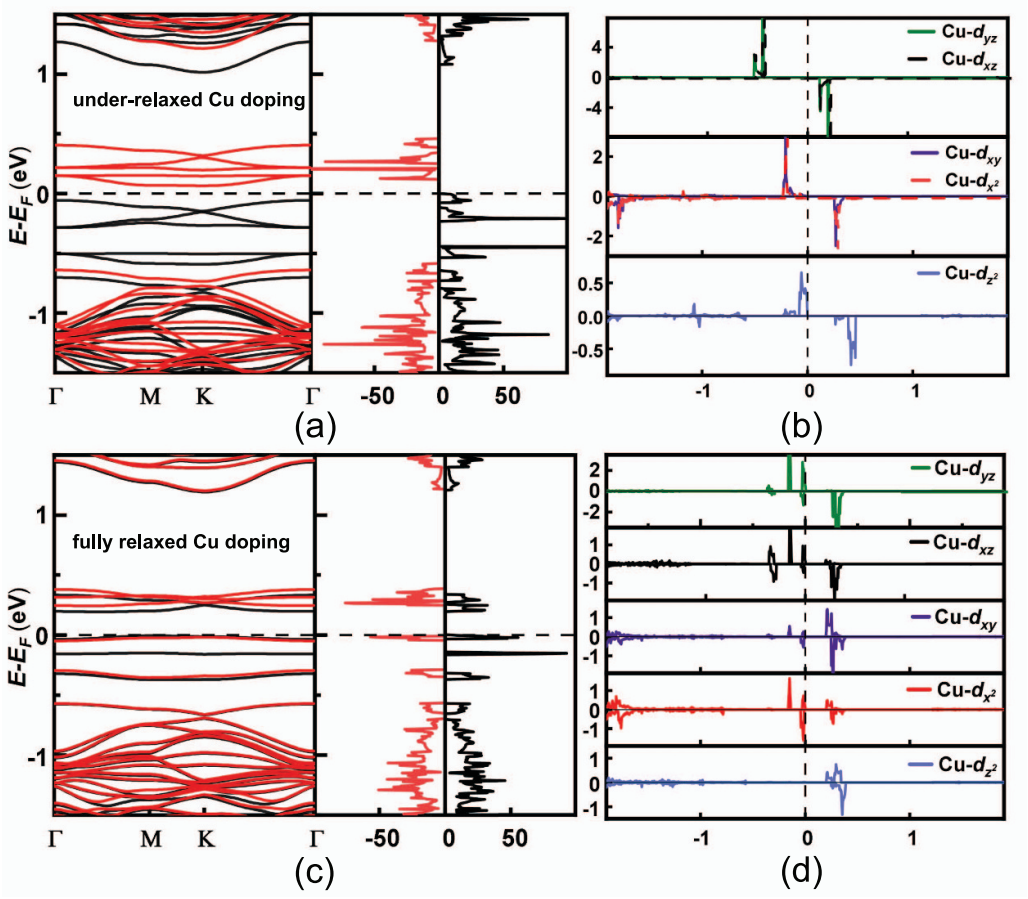

Figure 4. (a) and (c) Show band structures and DOSs for an under-relaxed and a fully relaxed Cu-doped monolayer of MoS_2. (b) and (d) Show the *d*-orbital PDOS of an under-relaxed and a fully relaxed Cu-doped monolayer of MoS_2.

supercell). In various configurations of V, Ni, and N doping, the results indicate non-magnetic behavior, making it difficult to achieve ferromagnetic order in these systems. For Mn-doped MoS_2, the calculations show ferromagnetic coupling in all tested configurations. In Fe-doped MoS_2, ferromagnetic coupling is observed in the first, second, and fourth nearest-neighbor configurations, while the third nearest-neighbor configuration exhibits antiferromagnetic coupling. Of note, we notice that the magnetic moment of the doped systems could be sensitive to the distribution of dopants. For instance, Fe dopants exhibit a spin-state transition from low-spin at shorter interatomic distances to high-spin in the fourth-nearest neighbor configuration. Our theoretical analysis indicates that the evolution of magnetic moments with doping configuration arises from the interplay between crystal field effects and exchange interactions, combined with significant band broadening effects. For Cu-doped MoS_2, ferromagnetic coupling occurs in the first and fourth nearest neighbors, but the second and third nearest-neighbor configurations are non-magnetic. Additionally, in all configurations of these six dopants, stability is found in the nearest-neighbor configurations, and as the distance between the dopant atoms increases, the energy of the system also increases, suggesting that all six dopants tend to cluster. Through theoretical calculations of the magnetic coupling between two dopant atoms, it can at least be concluded that the introduction of magnetism in V, Ni, and N-doped monolayer MoS_2 is unlikely. Many theoretical simulations [54, 66, 72, 99–102] that investigate the regulation of 2D materials' magnetism through heteroatom doping focus solely on the localized magnetic moments of the dopant atoms, without considering the magnetic coupling between them. This makes it difficult to ensure that the doped system exhibits macroscopic ferromagnetism.

In the study of magnetic regulation in 2D TMDCs (such as monolayer MoS_2), experimental reports have indicated that doping with V [103, 104], Mn [34, 35, 105], Fe [20, 106, 107], Ni [49], Cu [108, 109], and N [110] can induce ferromagnetic responses. However, our systematic analysis reveals that in some of these studies, the hysteresis loops of the ferromagnetic responses are notably small, and in others, the doping concentrations far exceed the limits of thermal equilibrium concentrations. These discrepancies raise concerns about the validity of the experimental results. We question whether the observed significant hysteresis loops are intrinsic properties of the doped systems or rather a consequence of secondary phase formation during the doping process. Consequently,

Table 2. The optimized total magnetic moments (M_{tot}), relative stability energy (E_{RS}) and magnetically ground state for each C_i structure of the two-impurity-doped MoS_2. The relative stability energy refers to the lowest energy of C_i structure in its ground state.

Impurity	C_i	M_{tot} (μ_B)	E_{RS} (eV)	Magnetic state
V	1st n.n.	0	0	NM
	2nd n.n.	0	0.11	NM
	3rd n.n.	0	0.111	NM
	4th n.n.	0	0.131	NM
Mn	1st n.n.	2	0	FM
	2nd n.n.	2	0.39	FM
	3rd n.n.	2	0.451	FM
	4th n.n.	2	0.502	FM
Fe	1st n.n.	2	0	FM
	2nd n.n.	2	0.759	FM
	3rd n.n.	0	0.871	AFM
	4th n.n.	4	0.871	FM
Ni	1st n.n.	0	0	NM
	2nd n.n.	0	1.291	NM
	3rd n.n.	0	1.38	NM
	4th n.n.	0	1.548	NM
Cu	1st n.n.	2	0	FM
	2nd n.n.	0	1.638	NM
	3rd n.n.	0	1.559	NM
	4th n.n.	2	2.051	FM
N	1st n.n.	0	0	NM
	2nd n.n.	0	0.071	NM
	3rd n.n.	0	0.153	NM
	4th n.n.	0	0.252	NM
	5th n.n.	0	0.837	NM
	6th n.n.	0	0.018	NM
	7th n.n.	0	0.035	NM
	8th n.n.	0	0.125	NM

we emphasize that rigorous material characterization is imperative in experimental investigations aimed at modulating the magnetic and spintronic properties of nonmagnetic materials through doping approaches.

3. Summary and future perspectives

We focus on the doping of monolayer MoS_2 with six elements-V, Mn, Fe, Ni, Cu, and N-as a case study to evaluate the feasibility of regulating magnetism through doping. The analysis is structured around three key aspects. First, we assess the thermal stability of the doped system, ruling out the possibility of high-concentration doping for Fe, Ni, and Cu in monolayer MoS_2. Second, we examine the electronic structure stability and dismiss the likelihood of Ni doping introducing localized magnetic moments. Finally, we analyze the magnetic coupling between dopant atoms, excluding the potential for V, Ni, and N doping to induce long-range magnetic order in MoS_2. Based on theoretical simulations, we conclude that of the six dopants, Mn-doped MoS_2 shows the greatest potential for successful magnetic regulation, though the issue of dopant atom aggregation must still be addressed [90]. This highlights the considerable challenges associated with regulating the magnetism of 2D non-magnetic materials through heteroatom doping, and it explains the fundamental reasons for the discrepancies between theoretical simulations and experimental findings. We strongly recommend that future theoretical studies account for these three critical factors.

Although significant efforts have been devoted to investigating and modulating the magnetic properties of 2D materials, the understanding of 2D ferromagnetism remains in its early stages. Compared to intrinsic 2D ferromagnets, defect- and doping-mediated 2D ferromagnetic materials typically exhibit superior air stability without requiring additional encapsulation processes. Moreover, these materials demonstrate better compatibility with existing wafer-scale synthesis techniques, facilitating industrial-scale production. However, before practical applications can be realized, several challenges beyond these three key factors must still be addressed. The magnetic properties induced by defects and doping are highly sensitive to multiple influencing factors, including defect type

and concentration, distribution uniformity, dopant elements, and temperature. Therefore, exploring and optimizing structural engineering and doping strategies to induce ferromagnetism in non-magnetic 2D materials will be a crucial direction for future research. Furthermore, after successfully introducing ferromagnetism, efforts should focus on integrating magnetic properties with other intrinsic characteristics (such as electrical, optical, and catalytic properties), thereby enabling broader applications in magnetoelectric coupling, magneto-optical interactions, and magnetocatalytic fields.

Data availability statement

All data that support the findings of this study are included within the article (and any supplementary files).

Acknowledgments

This work is financially supported by the National Natural Science Foundation of China (Grant No. 12474229). This work is partially supported by High Performance Computing Platform of South China University of Technology.

Appendix A. Computational details

All calculations in this study were performed using the VASP simulation package [111], which employs the projector-augmented wave approach [112] of density functional theory [113, 114]. The exchange-correlation interactions were treated using the generalized gradient approximation with the Perdew–Burke–Ernzerhof functional [115]. Initially, variations in defect formation energy and thermodynamic equilibrium concentration were examined across different supercell sizes, as illustrated in figure 5. Notably, the defect formation energy and concentration exhibited convergence within the $5 \times 5 \times 1$ supercell model. Consequently, all computational simulations were conducted using this $5 \times 5 \times 1$ supercell. The reciprocal space integrations were sampled with a k-mesh of $4 \times 4 \times 1$, generated by the Γ-centered Monkhorst–Pack method [116]. A vacuum layer of 15 Å was incorporated in our slab calculations to mitigate interactions between the slabs. The cutoff energy for the plane waves was set at 520 eV. All structures were relaxed using the conjugate gradient method until the maximum Hellmann–Feynman force acting on each atom was reduced to less than 0.01 eV $Å^{-1}$. For the self-consistent cycle, an energy criterion of 1×10^{-8} eV was employed.

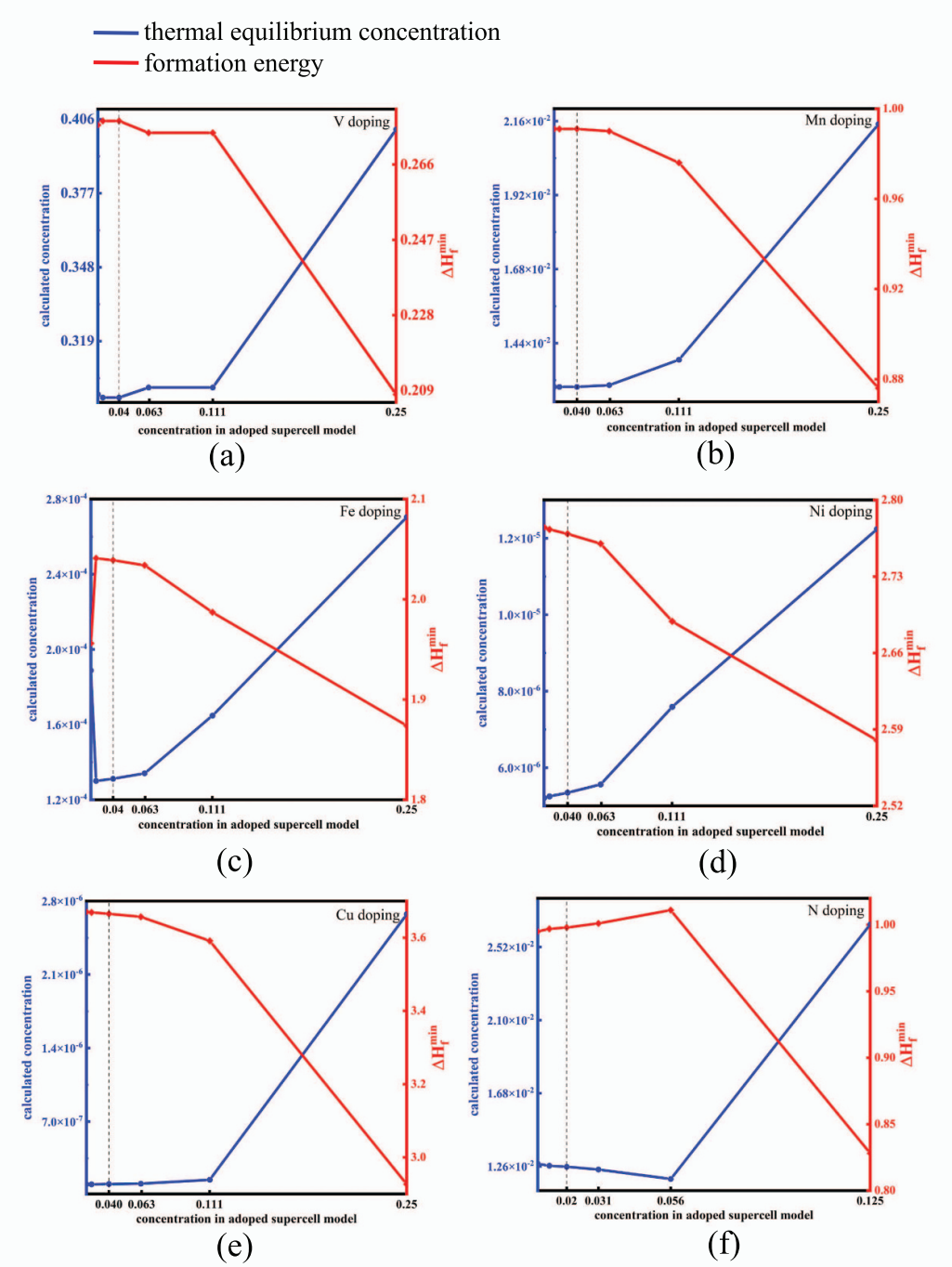

Figure 5. The computational results for monolayer MoS_2 doped with transition metals (V, Mn, Fe, Ni, Cu) and nitrogen (N) are presented in panels (a) through (f). The red curves denote the minimum defect formation energies derived from the doped supercell models, while the blue curves reflect the thermodynamic maximum site equilibrium concentrations of dopants calculated based on the defect formation energies.

Appendix B

Table B1. The summary of magnetic manipulation by heteroatom doping in nonmagnetic 2D materials.

Methods	Materials	Synthesis/Theory	Magnetic State	Reference
V doping	V-doped MoS_2	theoretical simulation	ferromagnetism	[46, 47, 117]
	V-doped MoS_2	theoretical simulation	nonavailable (NA)	[53, 54, 72]
	V-doped MoS_2	hydrothermal	ferromagnetism	[103]
	V-doped MoS_2	chemical vapor deposition (CVD)	ferromagnetism	[104]
	V-doped InS	theoretical simulation	ferromagnetism	[67]
	V-doped SnS_2/ V-doped ZrS_2	theoretical simulation	ferromagnetism	[86]
	V-doped $MoSe_2$	theoretical simulation	ferromagnetism	[47]
	V-doped $MoTe_2$	theoretical simulation	ferromagnetism	[78]
	V-doped $MoTe_2$	CVD	ferromagnetism	[118]
	V-doped ZrS_2	theoretical simulation	ferromagnetism	[119]
	V-doped WS_2	theoretical simulation	ferromagnetism	[47, 120]
	V-doped WS_2	single-stepfilm	ferromagnetism	[121]
	V-doped WS_2	CVD	ferromagnetism	[122]
	V-doped WSe_2	theoretical simulation	ferromagnetism	[47, 123]
	V-doped WSe_2	CVD	ferromagnetism	[122, 124, 125]
	V-doped $SnSe_2$	theoretical simulation	ferromagnetism	[73]
	V-doped InSe	theoretical simulation	ferromagnetism	[126]
	V-doped $HfSe_2$	theoretical simulation	ferromagnetism	[127]
	V-doped $MgCl_2$	theoretical simulation	NA	[84]
	V-doped MoSeTe	theoretical simulation	NA	[128]
	V-doped $PtTe_2$	theoretical simulation	ferromagnetism	[79]
	V-doped InP3	theoretical simulation	ferromagnetism	[82]
Cr doping	Cr-doped MoS_2	theoretical simulation	NA	[54]
	Cr-doped MoS_2	hydrothermal	ferromagnetism	[129]
	Cr-doped InS	theoretical simulation	ferromagnetism	[67]
	Cr-doped SnS_2	theoretical simulation	ferromagnetism	[86]
	Cr-doped $MoTe_2$	theoretical simulation	ferromagnetism	[78]
	Cr-doped $MoTe_2$	tellurium flux	ferromagnetism	[130]
	Cr-doped InSe	theoretical simulation	ferromagnetism	[126]
	Cr-doped $HfSe_2$	theoretical simulation	ferromagnetism	[127]
	Cr-doped $SnSe_2$	theoretical simulation	ferromagnetism	[73]
	Cr-doped WTe_2	Te flux strategy	ferromagnetism	[131]
	Cr-doped ZrS_2	theoretical simulation	ferromagnetism	[119]
	Cr-doped $MgCl_2$	theoretical simulation	NA	[84]
Mn doping	Mn-doped MoS_2	theoretical simulation	ferromagnetism	[40, 46, 47, 51, 66, 90, 91, 132]
	Mn-doped MoS_2	theoretical simulation	NA	[53, 54]
	Mn-doped MoS_2	hydrothermal	ferromagnetism	[34, 105]
	Mn-doped $MoSe_2$	theoretical simulation	ferromagnetism	[47, 132]
	Mn-doped $MoSe_2$	molecular beam epitaxy (MBE)	ferromagnetism	[133]
	Mn-doped $MoTe_2$	theoretical simulation	ferromagnetism	[78, 132]
	Mn-doped WS_2	theoretical simulation	ferromagnetism	[47, 77, 132, 134–136]
	Mn-doped WS_2	CVD	ferromagnetism	[35]
	Mn-doped WSe_2	theoretical simulation	ferromagnetism	[137]
	Mn-doped $HfSe_2$	theoretical simulation	ferromagnetism	[127]
	Mn-doped WSe_2	theoretical simulation	ferromagnetism	[47, 138, 139]
	Mn-doped $MgCl_2$	theoretical simulation	NA	[84]
	Mn-doped MoSeTe	theoretical simulation	NA	[128]
	Mn-doped AlN	theoretical simulation	ferromagnetism	[140]
Fe doping	Fe-doped MoS_2	theoretical simulation	ferromagnetism	[40, 46, 47, 141]
	Fe-doped MoS_2	theoretical simulation	NA	[53, 54, 72, 89]
	Fe-doped MoS_2	hydrothermal	ferromagnetism	[107]
	Fe-doped MoS_2	CVD	ferromagnetism	[20, 104, 106]

(Continued.)

Table B1. (Continued.)

Methods	Materials	Synthesis/Theory	Magnetic State	Reference
	Fe-doped MoS_2	hydrothermal	ferromagnetism	[49]
	Fe-doped MoS_2	spin coating and thermal decomposition	ferromagnetism	[142]
	Fe-doped $MoSe_2$	theoretical simulation	ferromagnetism	[47]
	Fe-doped $MoSe_2$	CVD	ferromagnetism	[143]
	Fe-doped $MoTe_2$	theoretical simulation	ferromagnetism	[78]
	Fe-doped ZrS_2	theoretical simulation	ferromagnetism	[119]
	Fe-doped SnS_2	theoretical simulation	ferromagnetism	[86]
	Fe-doped WS_2	theoretical simulation	ferromagnetism	[47, 77, 88, 144]
	Fe-doped WS_2	theoretical simulation	NA	[102]
	Fe-doped SnS_2	micro-mechanical cleavage	ferromagnetism	[145]
	Fe-doped WSe_2	theoretical simulation	ferromagnetism	[47, 137–139]
	Fe-doped InSe	theoretical simulation	ferromagnetism	[126]
	Fe-doped $SnSe_2$	theoretical simulation	ferromagnetism	[73]
	Fe-doped In_2Se_3	CVD	ferromagnetism	[146]
	Fe-doped $HfSe_2$	theoretical simulation	ferromagnetism	[127]
	Fe-doped graphdiyne	chemical reduction heat-treatment	ferromagnetism	[147]
	Fe-doped $MgCl_2$	theoretical simulation	NA	[84]
	Fe-doped MoSeTe	theoretical simulation	NA	[128]
	Fe-doped InP_3	theoretical simulation	ferromagnetism	[82]
Co doping	Co-doped MoS_2	theoretical simulation	ferromagnetism	[40, 46–48]
	Co-doped MoS_2	theoretical simulation	NA	[53, 54, 72]
	Co-doped MoS_2	hydrothermal	ferromagnetism	[49, 50]
	Co-doped $MoSe_2$	theoretical simulation	ferromagnetism	[47]
	Co-doped $MoSe_2$	CVD	ferromagnetism	[143]
	Co-doped $MoTe_2$	theoretical simulation	ferromagnetism	[78]
	Co-doped WS_2	theoretical simulation	ferromagnetism	[47, 77, 88, 144]
	Co-doped ZrS_2	theoretical simulation	ferromagnetism	[119]
	Co-doped WSe_2	theoretical simulation	ferromagnetism	[47, 137, 139]
	Co-doped graphene	impregnation-pyrolysis	ferromagnetism	[148]
	Co-doped phosphorene	theoretical simulation	ferromagnetism	[149]
	Co-doped ZnO	solution-based template-assisted	ferromagnetism	[150]
	Co-doped $MgCl_2$	theoretical simulation	NA	[84]
	Co-doped MoSeTe	theoretical simulation	NA	[128]
Ni doping	Ni-doped MoS_2	theoretical simulation	ferromagnetism	[74, 151]
	Ni-doped MoS_2	theoretical simulation	NA	[72]
	Ni-doped MoS_2	hydrothermal	ferromagnetism	[49]
	Ni-doped $MoSe_2$	CVD	ferromagnetism	[143]
	Ni-doped WS_2	theoretical simulation	ferromagnetism	[69, 77, 152]
	Ni-doped WSe_2	theoretical simulation	ferromagnetism	[139]
	Ni-doped WSe_2	chemical vapor transport (CVT)	ferromagnetism	[153]
	Ni-doped h-BN	theoretical simulation	ferromagnetism	[154]
	Ni-doped AlN	theoretical simulation	ferromagnetism	[140]
	Ni-doped $MgCl_2$	theoretical simulation	NA	[84]
	Ni-doped CoO	CVD	ferromagnetism	[155]
	Ni-doped MoSeTe	theoretical simulation	NA	[128]
Cu doping	Cu-doped MoS_2	theoretical simulation	ferromagnetism	[46]
	Cu-doped MoS_2	theoretical simulation	NA	[72]
	Cu-doped MoS_2	ion implantation	ferromagnetism	[108]
	Cu-doped MoS_2	hydrothermal	ferromagnetism	[109]
	Cu-doped $MoSe_2$	theoretical simulation	ferromagnetism	[71]
	Cu-doped WS_2	theoretical simulation	ferromagnetism	[77, 156]
	Cu-doped WSe_2	theoretical simulation	ferromagnetism	[129, 139]
	Cu-doped $PtTe_2$	theoretical simulation	ferromagnetism	[79]

(Continued.)

Table B1. (Continued.)

Methods	Materials	Synthesis/Theory	Magnetic State	Reference
Ti doping	Ti-doped WSe_2	theoretical simulation	ferromagnetism	[139]
	Ti-doped InSe	theoretical simulation	ferromagnetism	[126]
	Ti-doped InS	theoretical simulation	ferromagnetism	[67]
	Ti-doped black phosphorus	high pressure synthesis	ferromagnetism	[157]
	Ti-doped InP_3	theoretical simulation	ferromagnetism	[82]
Zn doping	Zn-doped MoS_2	theoretical simulation	ferromagnetism	[51]
	Zn-doped MoS_2	theoretical simulation	NA	[72]
	Zn-doped WS_2	theoretical simulation	ferromagnetism	[77]
	Zn-doped WSe_2	theoretical simulation	ferromagnetism	[139]
	Zn-doped $PtTe_2$	theoretical simulation	ferromagnetism	[79]
Nb doping	Nb-doped MoS_2	theoretical simulation	NA	[53]
	Nb-doped WS_2	theoretical simulation	ferromagnetism	[120]
	Nb-doped SnS_2	theoretical simulation	ferromagnetism	[81]
Ta doping	Ta-doped MoS_2	theoretical simulation	NA	[53]
	Ta-doped $MoTe_2$	CVT	ferromagnetism	[158]
	Ta-doped WS_2	theoretical simulation	ferromagnetism	[120]
	Re-doped MoS_2	theoretical simulation	ferromagnetism	[159]
	Re-doped MoS_2	CVD	ferromagnetism	[56]
	Re-doped MoS_2	hydrothermal annealing	ferromagnetism	[160]
Li doping	Li-doped ZrS_2	theoretical simulation	ferromagnetism	[119]
	Li-doped AlN	theoretical simulation	ferromagnetism	[161]
Na doping	Na-doped AlN	theoretical simulation	ferromagnetism	[161]
K doping	K-doped AlN	theoretical simulation	ferromagnetism	[161]
Al doping	Al-doped MoS_2	theoretical simulation	NA	[53]
Ga doping	Ga-doped MoS_2	theoretical simulation	NA	[53]
Mo doping	Mo-doped ZrS_2	theoretical simulation	ferromagnetism	[119]
	Mo-doped SnS_2	theoretical simulation	ferromagnetism	[81]
	Mo-doped $CrCl_3$/ Mo-doped $CrBr_3$	theoretical simulation	ferromagnetism	[68]
Cd doping	Cd-doped MoS_2	theoretical simulation	ferromagnetism	[51]
Te doping	Te-doped MoO_3	vapor-phase epitaxy	ferromagnetism	[18]
Bi doping	Bi-doped InSe	theoretical simulation	ferromagnetism	[162]
Noble metal doping	Hg-doped MoS_2	theoretical simulation	ferromagnetism	[51]
	Ru-doped WS_2/ Os-doped WS_2	theoretical simulation	NA	[102]
	Pd-doped WS_2	theoretical simulation	ferromagnetism	[69]
	Rh-doped ZnO/ Ru-doped ZnO	theoretical simulation	ferromagnetism	[101]
Rare earth doping	Sm-doped MoS_2/ Eu-doped MoS_2/ Gd-doped MoS_2/ Tb-doped MoS_2/ Dy-doped MoS_2	theoretical simulation	ferromagnetism	[52]
	Gd-doped MoS_2	theoretical simulation	ferromagnetism	[163]
	Dy-doped MoS_2	gas–liquid chemical deposition	ferromagnetism	[164]
	Ho-doped SnS_2	chemical gas–liquid phase deposition	ferromagnetism	[165]
	Nd-doped ZnO	theoretical simulation	ferromagnetism	[166]

(Continued.)

Table B1. (Continued.)

Methods	Materials	Synthesis/Theory	Magnetic State	Reference
Sc doping	Sc-doped WSe_2	theoretical simulation	ferromagnetism	[139]
Nonmetallic elements doping	B-doped MoS_2/ N-doped MoS_2/ P-doped MoS_2/ As-doped MoS_2	theoretical simulation	NA	[53]
	H-doped MoS_2/ B-doped MoS_2/ N-doped MoS_2/ F-doped MoS_2	theoretical simulation	NA	[54]
	N-doped MoS_2	CVD	ferromagnetism	[110]
	N-doped GaS	theoretical simulation	ferromagnetism	[167]
	N-doped ReS_2	Hydrothermal	ferromagnetism	[168]
	H-doped $MoSe_2$/ B-doped $MoSe_2$/ N-doped $MoSe_2$/ P-doped $MoSe_2$/ F-doped $MoSe_2$/ Cl-doped $MoSe_2$/ Br-doped $MoSe_2$/ I-doped $MoSe_2$	theoretical simulation	NA	[99]
	N-doped WSe_2/ P-doped WSe_2/ F-doped WSe_2/ Cl-doped WSe_2	theoretical simulation	NA	[100]
	C-doped $MgCl_2$/ N-doped $MgCl_2$/ O-doped $MgCl_2$	theoretical simulation	NA	[84]
	N-doped $PtTe_2$/ P-doped $PtTe_2$/ As-doped $PtTe_2$	theoretical simulation	ferromagnetism	[79]
	N-deoped g-ZnO	theoretical simulation	NA	[76]
	As-doped SnO	theoretical simulation	ferromagnetism	[162]
	C-doped BN	thermal degradation	ferromagnetism	[62]
	S-doped graphene	thermal exfoliation	ferromagnetism	[61]
	N-doped graphene	thermal exfoliation	ferromagnetism	[169]
	S-doped phosphorene/ Cl-doped phosphorene/ Si-doped phosphorene	theoretical simulation	NA	[85]
	S-doped graphdiyne	thermal sulfurization	ferromagnetism	[170]

ORCID iD

Yu-Jun Zhao https://orcid.org/0000-0002-6923-1099

References

[1] Cao Q, Lü W, Wang X R, Guan X, Wang L, Yan S, Wu T and Wang X 2020 *ACS Appl. Mater. Interfaces* **12** 42449–71
[2] Choudhuri I, Bhauriyal P and Pathak B 2019 *Chem. Mater.* **31** 8260–85
[3] Xia B, Gao D and Xue D 2021 *Nanoscale* **13** 12772–87
[4] Li H, Ruan S and Zeng Y J 2019 *Adv. Mater.* **31** 1900065
[5] Novoselov K S, Geim A K, Morozov S V, Jiang D E, Zhang Y, Dubonos S V, Grigorieva I V and Firsov A A 2004 *Science* **306** 666–9
[6] Gong C *et al* 2017 *Nature* **546** 265–9
[7] Deng Y *et al* 2018 *Nature* **563** 94–99
[8] Seo J *et al* 2020 *Sci. Adv.* **6** eaay8912
[9] Huang B *et al* 2017 *Nature* **546** 270–3
[10] Zhang Z, Shang J, Jiang C, Rasmita A, Gao W and Yu T 2019 *Nano Lett.* **19** 3138–42
[11] Mermin N D and Wagner H 1966 *Phys. Rev. Lett.* **17** 1133
[12] González-Herrero H, Gómez-Rodríguez J M, Mallet P, Moaied M, Palacios J J, Salgado C, Ugeda M M, Veuillen J Y, Yndurain F and Brihuega I 2016 *Science* **352** 437–41
[13] Nair R, Sepioni M, Tsai I L, Lehtinen O, Keinonen J, Krasheninnikov A V, Thomson T, Geim A and Grigorieva I 2012 *Nat. Phys.* **8** 199–202
[14] Avsar A, Ciarrocchi A, Pizzochero M, Unuchek D, Yazyev O V and Kis A 2019 *Nat. Nanotechnol.* **14** 674–8
[15] Wang Z, Tang C, Sachs R, Barlas Y and Shi J 2015 *Phys. Rev. Lett.* **114** 016603
[16] Ghiasi T S, Kaverzin A A, Dismukes A H, de Wal D K, Roy X and van Wees B J 2021 *Nat. Nanotechnol.* **16** 788–94

[17] Wei P *et al* 2016 *Nat. Mater.* **15** 711–6
[18] Lee D J, Lee Y, Kwon Y H, Choi S H, Yang W, Kim D Y and Lee S 2019 *ACS Nano* **13** 8717–24
[19] Saadaoui H *et al* 2016 *Phys. Rev. Lett.* **117** 227202
[20] Fu S *et al* 2020 *Nat. Commun.* **11** 2034
[21] Zhao X *et al* 2020 *Nature* **581** 171–7
[22] Li K, Chang T H, Xie Q, Cheng Y, Yang H, Chen J and Chen P Y 2019 *Adv. Electron. Mater.* **5** 1900040
[23] Kabiraj A and Mahapatra S 2019 *J. Phys. Chem. C* **124** 1146–57
[24] Wang Y, Morozov Y V, Zhukovskyi M, Chatterjee R, Draguta S, Tongying P, Bryant B, Rouvimov S and Kuno M 2016 *ACS Energy Lett.* **1** 175–81
[25] Feng Q, Tang N, Liu F, Cao Q, Zheng W, Ren W, Wan X and Du Y 2013 *ACS Nano* **7** 6729–34
[26] Tuček J *et al* 2017 *Nat. Commun.* **8** 14525
[27] López-Sancho M P, de Juan F and Vozmediano M A 2009 *Phys. Rev. B* **79** 075413
[28] Zhang Z, Zou X, Crespi V H and Yakobson B I 2013 *ACS Nano* **7** 10475–81
[29] Magda G Z, Jin X, Hagymási I, Vancsó P, Osváth Z, Nemes-Incze P, Hwang C, Biro L P and Tapasztó L 2014 *Nature* **514** 608–11
[30] Yazyev O V and Katsnelson M 2008 *Phys. Rev. Lett.* **100** 047209
[31] Averyanov D V, Sokolov I S, Tokmachev A M, Parfenov O E, Karateev I A, Taldenkov A N and Storchak V G 2018 *ACS Appl. Mater. Interfaces* **10** 20767–74
[32] Bointon T H, Khrapach I, Yakimova R, Shytov A V, Craciun M F and Russo S 2014 *Nano Lett.* **14** 1751–5
[33] Sokolov I S, Averyanov D V, Parfenov O E, Taldenkov A N, Karateev I A, Tokmachev A M and Storchak V G 2021 *J. Alloys Compd.* **884** 161078
[34] Wang J, Sun F, Yang S, Li Y, Zhao C, Xu M, Zhang Y and Zeng H 2016 *Appl. Phys. Lett.* **109** 092401
[35] Li Y, Cheng X, Zhao Y, Liu M, Li F, Huang C, Dai L, Wan Y and Kan E 2023 *J. Phys. Chem. C* **127** 12648–54
[36] Saha S, Bañobre-López M, Bondarchuk O, Fernández-Rossier J and Deepak F L 2021 *J. Mater. Sci.* **56** 9692–701
[37] Wang Q H, Kalantar-Zadeh K, Kis A, Coleman J N and Strano M S 2012 *Nat. Nanotechnol.* **7** 699–712
[38] Ataca C, Sahin H, Akturk E and Ciraci S 2011 *J. Phys. Chem. C* **115** 3934–41
[39] Tongay S, Varnoosfaderani S S, Appleton B R, Wu J and Hebard A F 2012 *Appl. Phys. Lett.* **101** 123105
[40] Lin X and Ni J 2014 *J. Appl. Phys.* **116** 044311
[41] Tao P, Guo H, Yang T and Zhang Z 2014 *J. Appl. Phys.* **115** 054305
[42] Saab M and Raybaud P 2016 *J. Phys. Chem. C* **120** 10691–7
[43] Conley H J, Wang B, Ziegler J I, Haglund J R F, Pantelides S T and Bolotin K I 2013 *Nano Lett.* **13** 3626–30
[44] Lee H S, Min S W, Chang Y G, Park M K, Nam T, Kim H, Kim J H, Ryu S and Im S 2012 *Nano Lett.* **12** 3695–700
[45] Newaz A, Prasai D, Ziegler J I, Caudel D, Robinson S, Haglund Jr. J R F and Bolotin K I 2013 *Solid State Commun.* **155** 49–52
[46] Fan X L, An Y R and Guo W J 2016 *Nanoscale Res. Lett.* **11** 1–10
[47] Tiwari S, Van de Put M L, Sorée B and Vandenberghe W G 2021 *npj 2D Mater. Appl.* **5** 54
[48] Wang Y, Li S and Yi J 2016 *Sci. Rep.* **6** 24153
[49] Martinez L, Delgado J, Saiz C, Cosio A, Wu Y, Villagrán D, Gandha K, Karthik C, Nlebedim I and Singamaneni S 2018 *J. Appl. Phys.* **124** 153903
[50] Xiang Z, Zhang Z, Xu X, Zhang Q, Wang Q and Yuan C 2015 *Phys. Chem. Chem. Phys.* **17** 15822–8
[51] Cheng Y, Zhu Z, Mi W, Guo Z and Schwingenschlögl U 2013 *Phys. Rev. B* **87** 100401
[52] Majid A, Imtiaz A and Yoshiya M 2016 *J. Appl. Phys.* **120** 142124
[53] Lu S C and Leburton J P 2014 *Nanoscale Res. Lett.* **9** 1–9
[54] Yue Q, Chang S, Qin S and Li J 2013 *Phys. Lett. A* **377** 1362–7
[55] Krasheninnikov A, Lehtinen P, Foster A S, Pyykkö P and Nieminen R M 2009 *Phys. Rev. Lett.* **102** 126807
[56] Kochat V *et al* 2017 *Adv. Mater.* **29** 1703754
[57] Ahmed S, Ding X, Murmu P P, Bao N, Liu R, Kennedy J, Ding J and Yi J 2018 *J. Alloys Compd.* **731** 25–31
[58] Lee J U, Lee S, Ryoo J H, Kang S, Kim T Y, Kim P, Park C H, Park J G and Cheong H 2016 *Nano Lett.* **16** 7433–8
[59] Sui X, Si C, Shao B, Zou X, Wu J, Gu B L and Duan W 2015 *J. Phys. Chem. C* **119** 10059–63
[60] Li S, Ao Z, Zhu J, Ren J, Yi J, Wang G and Liu W 2017 *J. Phys. Chem. Lett.* **8** 1484–8
[61] Tuček J, Błoński P, Sofer Z, Šimek P, Petr M, Pumera M, Otyepka M and Zbořil R 2016 *Adv. Mater.* **28** 5045–53
[62] Zhao C, Xu Z, Wang H, Wei J, Wang W, Bai X and Wang E 2014 *Adv. Funct. Mater.* **24** 5985–92
[63] Onofrio N, Guzman D and Strachan A 2017 *J. Appl. Phys.* **122** 185102
[64] Zhang S, Wei S H and Zunger A 1997 *Phys. Rev. Lett.* **78** 4059
[65] Zhang S, Wei S H, Zunger A and Katayama-Yoshida H 1998 *Phys. Rev. B* **57** 9642
[66] Mekonnen Hailemariam S 2020 *Adv. Condens. Matter Phys.* **2020** 9635917
[67] Xue R, Han R, Lin X and Wu P 2023 *Appl. Surf. Sci.* **608** 155240
[68] Safi A, Chakraborty S, Ahmed M A, Panda S and Chattopadhyay B 2023 *ECS J. Solid State Sci. Technol.* **12** 043001
[69] Zhao X, Xia C, Wang T and Dai X 2016 *J. Alloys Compd.* **654** 574–9
[70] Ouettar C, Yahi H and Chibani H 2022 *J. Magn. Magn. Mater.* **551** 169163
[71] Hu A M, Wang L l, Xiao W Z and Meng B 2015 *Physica E* **73** 69–75
[72] Yun W S and Lee J 2014 *Phys. Chem. Chem. Phys.* **16** 8990–6
[73] Wu X, Han J, Feng Y, Li G, Wang C, Ding G and Gao G 2017 *RSC Adv.* **7** 44499–504
[74] Luo M, Shen Y H and Chu J H 2016 *Jpn. J. Appl. Phys.* **55** 093001
[75] Rong Q Y, Xiao W Z, Xiao G, Hu A M and Wang L L 2016 *J. Alloys Compd.* **674** 463–9
[76] Bing-Quan H, Tie-Ge Z, Dao-Xiong W, Zhao-Fu Z and Bai-Kui L 2019 *Acta Phys. Sin.* **68** 24
[77] Yang Y, Fan X L and Zhang H 2016 *Comput. Mater. Sci.* **117** 354–60
[78] Kanoun M B 2018 *J. Alloys Compd.* **748** 938–42
[79] Chen W, Zhang J M, Wang X G, Xia Q L, Nie Y Z and Guo G H 2021 *J. Magn. Magn. Mater.* **518** 167433
[80] Wu C W, Huang J H and Yao D X 2019 *J. Magn. Magn. Mater.* **469** 306–14
[81] Xiao W Z, Xiao G, Rong Q Y, Chen Q and Wang L L 2017 *J. Magn. Magn. Mater.* **438** 152–62
[82] Zhang M, Guo H M, Lv J, Jia J F and Wu H S 2021 *J. Magn. Magn. Mater.* **533** 168026
[83] Huy H A, Nguyen D K, Ponce-Pérez R, Guerrero-Sanchez J and Hoat D 2023 *Mater. Today Commun.* **36** 106511
[84] Lima I T, Vasconcelos R, Gargano R and Paura E N 2020 *New J. Chem.* **44** 8833–9
[85] Khan I and Hong J 2015 *New J. Phys.* **17** 023056
[86] Ao L, Pham A, Xiao H, Zu X and Li S 2016 *Phys. Chem. Chem. Phys.* **18** 25151–60

[87] Hu A M, Wang L l, Meng B and Xiao W Z 2015 *Solid State Commun.* **220** 67–71
[88] Hyun J M and Kim M 2018 *IEEE Trans. Magn.* **55** 1–4
[89] Lan L, Cao J M, Cao Y J, Xu D S and Zhou J 2015 *Key Eng. Mater.* **645** 15–20
[90] Ramasubramaniam A and Naveh D 2013 *Phys. Rev. B* **87** 195201
[91] Gao B, Huang C, Zhu F, Ma C L and Zhu Y 2021 *Phys. Lett. A* **414** 127636
[92] Wilson J A and Yoffe A 1969 *Adv. Phys.* **18** 193–335
[93] Enyashin A, Gemming S and Seifert G 2007 *Eur. Phys. J. Spec. Top.* **149** 103–25
[94] Böker T, Severin R, Müller A, Janowitz C, Manzke R, Voß D, Krüger P, Mazur A and Pollmann J 2001 *Phys. Rev. B* **64** 235305
[95] Li T and Galli G 2007 *J. Phys. Chem. C* **111** 16192–6
[96] Mattheiss L F 1973 *Phys. Rev. B* **8** 3719
[97] Coehoorn R, Haas C, Dijkstra J, Flipse C d, De Groot R and Wold A 1987 *Phys. Rev. B* **35** 6195
[98] Fleischauer P D, Lince J R, Bertrand P and Bauer R 1989 *Langmuir* **5** 1009–15
[99] Zhao Y, Wang W, Li C, Xu Y and He L 2018 *Solid State Commun.* **281** 6–11
[100] Zhang Y, Zhao Y, Xu Y and He L 2021 *Solid State Commun.* **327** 114233
[101] Hu H, Kang C, Xiong Z, Cui Y and Chen L 2023 *Mater. Today Commun.* **36** 106789
[102] Zhu Y-Y and Zhang J-M 2018 *Superlattices Microstruct.* **117** 155–62
[103] Ahmed S *et al* 2017 *Chem. Mater.* **29** 9066–74
[104] Tao R, Yang Z H, Tan C, Hao X, Ke Z G, Yang L, Dai L P, Deng X W, Li P J and Wang Z G 2022 *J. Electron. Sci. Technol.* **20** 100167
[105] Singh M K, Chettri P, Tripathi A, Tiwari A, Mukherjee B and Mandal R 2018 *Phys. Chem. Chem. Phys.* **20** 15817–23
[106] Kang K *et al* 2020 *Nanotechnology* **32** 095708
[107] Xia B, Yang Y, Ma J, Tao K and Gao D 2017 *Appl. Phys. Express* **10** 093002
[108] Zhang M, Li Q, Cheng W, Gao Y, Liao B and Ying M 2023 *Appl. Surf. Sci.* **608** 155220
[109] Xia B, Guo Q, Gao D, Shi S and Tao K 2016 *J. Phys. D: Appl. Phys.* **49** 165003
[110] Chen M, Hu C, Luo X, Hong A, Yu T and Yuan C 2020 *Appl. Phys. Lett.* **116** 073102
[111] Hafner J 2008 *J. Comput. Chem.* **29** 2044–78
[112] Blöchl P E 1994 *Phys. Rev. B* **50** 17953
[113] Hohenberg P and Kohn W 1964 *Phys. Rev.* **136** B864
[114] Kohn W and Sham L J 1965 *Phys. Rev.* **140** A1133
[115] Perdew J P, Burke K and Ernzerhof M 1996 *Phys. Rev. Lett.* **77** 3865
[116] Monkhorst H J and Pack J D 1976 *Phys. Rev. B* **13** 5188
[117] Mekonnen S and Singh P 2018 *Int. J. Mod. Phys. B* **32** 1850231
[118] Coelho P M, Komsa H P, Lasek K, Kalappattil V, Karthikeyan J, Phan M H, Krasheninnikov A V and Batzill M 2019 *Adv. Electron. Mater.* **5** 1900044
[119] Yang B, Zheng H, Han R, Du X and Yan Y 2014 *RSC Adv.* **4** 54335–43
[120] Li H, Liu S, Huang S, Yin D, Li C and Wang Z 2016 *Ceram. Int.* **42** 2364–9
[121] Zhang F *et al* 2020 *Adv. Sci.* **7** 2001174
[122] Yun S J, Duong D L, Ha D M, Singh K, Phan T L, Choi W, Kim Y M and Lee Y H 2020 *Adv. Sci.* **7** 1903076
[123] Duong D L, Yun S J, Kim Y, Kim S G and Lee Y H 2019 *Appl. Phys. Lett.* **115** 242406
[124] Pham Y T H, Liu M, Jimenez V O, Yu Z, Kalappattil V, Zhang F, Wang K, Williams T, Terrones M and Phan M H 2020 *Adv. Mater.* **32** 2003607
[125] Deng J, Zhou Z, Chen J, Cheng Z, Liu J and Wang Z 2022 *Chem. Phys. Chem.* **23** e202200162
[126] Li X, Xia C, Du J and Xiong W 2018 *J. Mater. Sci.* **53** 3500–8
[127] Zhao X, Yang C, Wang T, Ma X, Wei S and Xia C 2017 *RSC Adv.* **7** 52747–54
[128] Li Y, Qiu B, Zhao X, Hu G, Yue W, Yuan X and Ren J 2019 *Eur. Phys. J. B* **92** 1–6
[129] Zhang R, Du Y, Han G and Gao X 2019 *J. Mater. Sci.* **54** 552–9
[130] Yang L, Wu H, Zhang L, Zhang G, Li H, Jin W, Zhang W and Chang H 2021 *ACS Appl. Mater. Interfaces* **13** 31880–90
[131] Yang L *et al* 2021 *Adv. Funct. Mater.* **31** 2008116
[132] Mishra R, Zhou W, Pennycook S J, Pantelides S T and Idrobo J C 2013 *Phys. Rev. B* **88** 144409
[133] Dau M *et al* 2019 *APL Mater.* **7** 051111
[134] Zhao X, Dai X, Xia C, Wang T and Peng Y 2015 *Solid State Commun.* **215** 1–4
[135] Zhao X, Dai X, Xia C and Wang T 2015 *Superlattices Microstruct.* **85** 339–47
[136] Fang Q, Zhao X, Huang Y, Xu K, Min T, Chu P K and Ma F 2018 *Phys. Chem. Chem. Phys.* **20** 553–61
[137] Xie L Y and Zhang J M 2016 *Superlattices Microstruct.* **98** 148–57
[138] Gil C J, Pham A, Yu A and Li S 2014 *J. Phys.: Condens. Matter* **26** 306004
[139] Zhao X, Chen P and Wang T 2016 *Superlattices Microstruct.* **100** 252–7
[140] Wang S, An Y, Xie C, Zhang H and Zeng Q 2018 *Superlattices Microstruct.* **122** 171–80
[141] Shu H, Luo P, Liang P, Cao D and Chen X 2015 *ACS Appl. Mater. Interfaces* **7** 7534–41
[142] Kıvrak B, Akyol M and Ekicibil A 2022 *J. Mater. Sci. Mater. Electron.* **33** 16574–85
[143] Shen D *et al* 2022 *ACS Nano* **16** 10623–31
[144] Sun X, Yang K and Li Z 2022 *Phys. Status Solidi* **16** 2100611
[145] Li B, Xing T, Zhong M, Huang L, Lei N, Zhang J, Li J and Wei Z 2017 *Nat. Commun.* **8** 1958
[146] Yang H, Pan L, Xiao M, Fang J, Cui Y and Wei Z 2020 *Sci. China Mater.* **63** 421–8
[147] Zhang M, Wang X, Sun H, Yu J, Wang N, Long Y and Huang C 2018 *2D Mater.* **5** 035039
[148] Hu W *et al* 2021 *Nat. Commun.* **12** 1854
[149] Seixas L, Carvalho A and Castro Neto A 2015 *Phys. Rev. B* **91** 155138
[150] Chen R *et al* 2021 *Nat. Commun.* **12** 3952
[151] Han X, Benkraouda M, Qamhieh N and Amrane N 2020 *Chem. Phys.* **528** 110501
[152] Luo M, Hao S Y and Ling Y T 2016 *AIP Adv.* **6** 085112
[153] Habib M, Muhammad Z, Khan R, Wu C, Ur Rehman Z, Zhou Y, Liu H and Song L 2018 *Nanotechnology* **29** 115701
[154] Wang M, Tang S, Ren J, Wang B, Han Y and Dai Y 2018 *J. Supercond. Novel Magn.* **31** 1559–65
[155] Jiang J, Feng W, Wen Y, Yin L, Wang H, Feng X, Pei Y L, Cheng R and He J 2023 *Adv. Mater.* **35** 2301668
[156] Zhao X, Dai X and Xia C 2015 *Solid State Commun.* **217** 66–69
[157] Jiang X, Zhang X, Hua Z, Han D, Zhao W, Wang Z and Yang S 2019 *Phys. Lett. A* **383** 2097–101
[158] Yang L, Wu H, Zhang W, Lou X, Xie Z, Yu X, Liu Y and Chang H 2019 *Adv. Electron. Mater.* **5** 1900552
[159] Zhao P, Zheng J, Guo P, Jiang Z, Cao L and Wan Y 2017 *Comput. Mater. Sci.* **128** 287–93
[160] Xia B, Liu P, Liu Y, Gao D, Xue D and Ding J 2018 *Appl. Phys. Lett.* **113** 013101
[161] Xiao G, Wang L L, Rong Q Y, Hu A M and Xiao W Z 2016 *Phys. Status Solidi b* **253** 1816–23

[162] Houssa M, Meng R, Iordanidou K, Pourtois G, Afanas' ev V and Stesmans A 2021 *J. Comput. Electron.* **20** 88–94
[163] Zhang X, Wang X and Mi W 2015 *Solid State Commun.* **212** 35–40
[164] Zhao Q, Lu Q, Liu Y and Zhang M 2019 *Appl. Surf. Sci.* **471** 118–23
[165] Zhao Q, Zhang H, Liu Y, Zhu M and Zhang M 2019 *Appl. Surf. Sci.* **481** 1370–6
[166] Tan C, Sun D, Zhou L, Tian X and Huang Y 2016 *Superlattices Microstruct.* **98** 416–22
[167] Khan R, Rahman A U, Zhang Q, Kratzer P and Ramay S M 2021 *J. Phys.: Condens. Matter* **33** 314003
[168] Zhang Q, Ren Z, Wu N, Wang W, Gao Y, Zhang Q, Shi J, Zhuang L, Sun X and Fu L 2018 *npj 2D Mater. Appl.* **2** 22
[169] Błonski P, Tucek J, Sofer Z, Mazanek V, Petr M, Pumera M, Otyepka M and Zboril R 2017 *J. Am. Chem. Soc.* **139** 3171–80
[170] Zhang M, Sun H, Wang X, Du H, He J, Long Y, Zhang Y and Huang C 2019 *J. Phys. Chem. C* **123** 5010–6